Machine learning based prediction of channelisation during dissolution of carbonate rocks

Machine learning based prediction of channelisation during dissolution of carbonate rocks

F, Brondolo[1,2,3], P. A. Cilli[1,2,4], I. B. Butler[1,2], A. Fraser-Harris[1,2],K. Edlmann[1,2]and C. McDermott[1,2]

[1]School of Geosciences, University of Edinburgh, Edinburgh, UK
[2]International Centre for Carbonate Reservoirs, Edinburgh, UK
[3]Now at Stanford University - SLAC, Menlo Park, USA
[4]Now at Department of Earth Sciences, University of Oxford, Oxford, UK

Key Points:

- Artificial neural network
- Machine learning
- µCT
- Channels
- Carbonates

Corresponding author: F. Brondolo, brondolo@slac.stanford.edu

Abstract

Evolving preferential dissolution channels are common features formed during reactive fluid flow in carbonate rocks. Understanding these is of particular importance in applications involving subsurface engineered reservoirs but predicting their progression is currently challenging and poorly understood. Here, we propose a new approach to predict both the spatial distribution and extent of dissolution using a combination of experimental work, X-ray microtomography (µCT) and machine learning. We have conducted experiments, under reservoir conditions of temperature and pressure, involving pre- and post-flooding µCT characterisations, and coupled the outputs with a neural network to predict locations where carbonate was most likely to be dissolved. Our simulations demonstrate that our new solution can identify the key geometrical features that are important during dissolution, and can accurately predict the location and spread of dissolution. An important benefit of this approach is that it can accurately predict dissolution channels through forward prediction, while it does not require further chemical parameters, using instead common and accessible variables.

1 Introduction

Injection of fluid into carbonate reservoir rocks is a widely used process involved in subsurface engineered reservoirs to manage permeability and fluid flow (geothermal, groundwater management, carbon sequestration, enhanced oil recovery, etc.). The injected fluid creates changes in the fluid dynamic and stress state, leading to dissolution where the pore network, chemistry, temperature, fluid composition and pressures all influence the location, degree, and spread of the preferential channelling (Hoefner & Fogler, 1988; C. N. Fredd & Fogler, 1998; Golfier et al., 2002; Menke et al., 2017). The reactive and heterogeneous nature of carbonates make predictions of fluid behaviour challenging, and much work has been done on channelisation and classification in a variety of fluid-mineral systems as a function of the fluid flow rate and the fluid properties (Hoefner & Fogler, 1988; Steefel & Lasaga, 1990; Frick et al., 1994; Bazin et al., 1995; C. Fredd et al., 1996; C. N. Fredd & Fogler, 1998; Golfier et al., 2002; Walle et al., 2015), where fluid properties have been identified as largely controlling dissolution and channelisation in carbonates (Golfier et al., 2002). Numerical modelling studies have attempted to recreate these

dissolution processes by including variables influencing the general shape and spread of the dissolution footprint, such as system pressure, permeability, velocity of the fluid, or diffusion rate across boundary layers. Models have been tested, from a conceptual approach that considered a pre-existing cylindrical wormhole (Hung et al., 1989; Wang et al., 1993; Buijse et al., 1997; Huang et al., 1997, 1999), to more complex approaches focusing on the grain scale (Hoefner & Fogler, 1988; Daccord et al., 1989), on the fluid mechanics (Daccord, Lenormand, & Lietard, 1993; Daccord, Lietard, & Lenormand, 1993), or the mass and flow transfer (Liu et al., 1997; Chen et al., 1997). Most of these approaches displayed reasonable qualitative results of channel geometry and were backed by experimental outputs, against computationally expensive treatments operating over millimetre scale volumes. Here, we have coupled experimental work and Artificial Neural Networks (ANNs). The benefit of ANNs stems from the non-linear aspect of the solving algorithms coupled with their ability to learn and recognise patterns (Basheer & Hajmeer, 2000). Although studies have joined µCT imaging and machine learning as a segmentation tool for 3D volumes (Cortina-Januchs et al., 2011; Chauhan et al., 2016) and for rock modulus estimations (Sonmez et al., 2006), no work has been published on predictions of the spatial distribution of carbonate dissolution, purely relying on µCT images. Our approach has the advantage that it works as a predictive tool for channel spatial distribution, spread, and magnitude, over centimetre large volumes, in relatively short computational times. We have combined experimental data with an ANN to develop a predictive tool for preferential flow-path development.

The model presented in this study used datasets that were generated during experimental investigations of reactive fluid flow in carbonate samples. We investigated channels development through carbonate samples of heterogeneous nature by comparing the ANN computed solutions to 4 experimental results. For the experimental fluid flows, we used a range of flow rates and these have been named High Flow Rate 1 and 2 (HFR 1; HFR 2), Medium Flow Rate (MFR), and Low Flow Rate (LFR). Our coupled numerical work included a pre-processing of pre-experimentally tested core samples µCT-scans followed by a training of the ANN against the post-experimental channels data. The pre-experimental data - referred to as Input data - were based on 18 + 1 variables describing the geometrical attributes of the pore network (steps A and B in Figure 1). The differential result between pre- and post-

experimental µCT-scans allowed to pinpoint dissolution channels, leading to the generation of the Signature dataset (steps C and D in Figure 1). We trained multiple hidden layer ANNs on six datasets (including Input and Signature datasets) and blindly predicted on two (including the Input dataset only), corresponding to the four experimental regimes (further explained in Section 2.1). By doing so, we have been able to favourably predict the occurrence, shape, and magnitude of the dissolution pathways evolution in heterogeneous carbonate rocks using only attributes extracted from µCT scans, before flooding, on representative volumes. Moreover, the processing times of our solution were significantly smaller than the various computationally expensive systems models (Budek & Szymczak, 2012), with the non-negligible advantage of using larger cuboids inputs (Blunt et al., 2013; Bijeljic et al., 2004).

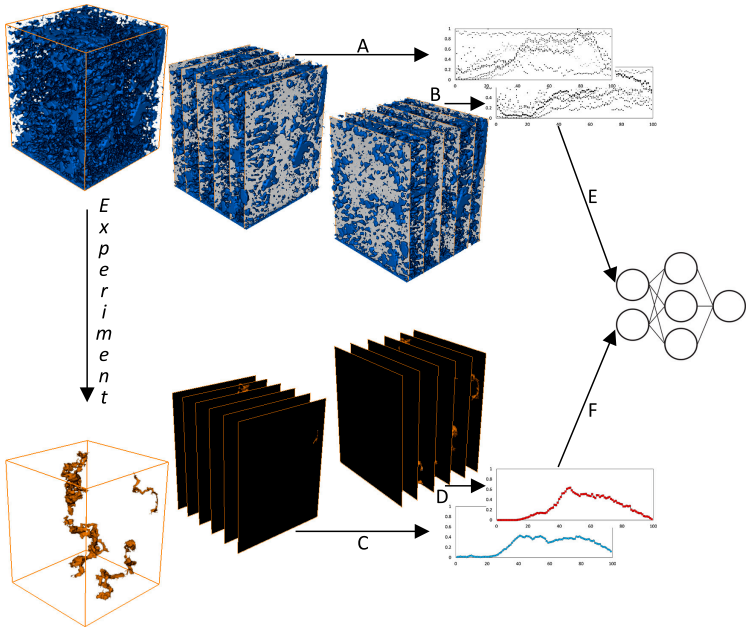

Figure 1: Data acquisition workflow. The two sub-sampled cuboids (pre-flooding and channels) are of the same size. Both stacks have been re-sliced a hundred times in two orthogonal directions. A & B: input data acquisition; C & D: signature data (or true solution) acquisition; E & F: input and signature data as attributes for the ANN.

2 Materials and Methods

2.1 Experimental matrix and dissolution regimes

The experimental dataset used to develop our methodology, and train and test the ANN, comprised a set of four experiments on highly heterogeneous - in porop-ermeability - travertine samples. Each core was 3.8 cm in diameter and differing in length (6.8 cm $<$ L $<$ 8.1 cm). The experimental procedure started with a pre-experimental preparation and conditioning of the core samples, followed by µCT acquisitions of the clean cores. The post-experimental process consisted of sonicating the samples in distilled water, before drying them for a week at 65 °C for one week, followed by post-experimental µCT acquisitions. The experimental flooding consisted in injecting an artificially made seawater of known pH (cf. supplementary information). The four experiments were carried under realistic geo-reservoir conditions of pressure and temperature (temperature T = 60 °C). The effective stress used in this study refers to the work of Terzaghi (1951), while the pore volume rate (PV_{rate}) used in this study is described by: $PV_{rate} = Q(t)/V_p$, with $Q(t)$ the amount of fluid injected per minute logged (m^3) and V_p the volume of pore of the rock sample (m^3). The porosity is calculated before the experiments, using the triple weighing technique (Luquot et al., 2016), and displays an average value of ∼11 % (from ∼5 % to ∼14 %). Table 1 presents the four experimental scenarios.

Experiment	Flow rate (cm^3/min)	PV_{rate} (-)	Eff. stress (MPa)	Conf. pressure (MPa)
HFR 1	15.58	2.6	10	50
HFR 2	14.25	2.5	40	50
MFR	6.24	1	10	50
LFR	1	0.2	40	50

Table 1: Flow rate, pore volume rate, effective pressure and confining pressure used for the four experimental floodings. Further petrophysical and chemical data on the rock samples are given in supplementary information.

2.2 µCT Processing

2.2.1 Data Acquisition

For each core, pre- and post-experimental flooding, tomographic data were acquired at 130 kV, and 25 W target power loading. Each dataset consists of 2,000 projections; each of 2 s duration, during a 360° revolution. Reconstruction by filtered back-projection used Octopus v8.7 software (Dierick et al., 2004), while post-processing data analysis and registrations of the pre- and post-flooding dataset of each rock, followed by the processing of the differences between both stacks were done using Fiji (Schindelin et al., 2012) and Avizo®9 functions.

2.2.2 Channel Resolution

The channels formed during our experimental fluid flooding can be detected through image processing by processing the difference between the pre- and post-experimental µCT volumes, while taking into account the initial porosity. The two types of datasets were generated. The first one represented the 3D volumes of pre-experimental scans - referred to as input data. These datasets were used for training the ANN and/or predicting the preferential pathway(s) location and magnitude. The second one were 3D volumes of dissolution channels - referred to as signature data. These datasets represent the true solution of channel(s) formation and were used for training the ANN.

As a way to account for the difference in samples sizes, we sub-sampled the 3D stacks into cuboids of variable side lengths (550 px to 650 px large) and constant axial length of 710 slices (∼2.5 cm by ∼2.9 cm). Both input and signature volumes of a single core sample are sub-sampled at the same location: To save further computational time, the 3D sub-sampled volumes were re-sliced a hundred times in two orthogonal directions - each sampled direction creating a dataset which we treated as independent - with respect to the axial axis and the original orientation of the sample within the sub-sampled core. Figure 1 presents the workflow for µCT data acquisition. In total, we have scanned four samples, translated into eight datasets, which were later divided into training & validation data (six datasets) and blind test data (two datasets) when developing the ANN.

2.3 Modelling

2.3.1 Input Data

The input data were a set of calculated geometric, physical, and simple statistical variables for predicting material loss during experimental floodings. Extraction of the information involved a conversion from the 16-bit grayscale 2D slices stacks to normalized 1D variables that can be evaluated by the ANN.

The formating of the input data has been done via a Visual Basic for Applications (VBA) batch coupled with Corel® X7 suite has been used as a quick way to apply the same formatting to each 2D slice. The batch automatically and sequentially thresholded, smoothed, vectorized, and resized each image to its original size.

For each formatted 2D slice, a set of nineteen relevant variables were collected through an in-depth image analysis. Most variables can easily be explained through image interpretation and simple mathematics (1, 6, 7, 9, 10, 13, 14, 15, 17), as well as variable 18 (PV_{rate}, cf. Section 2.1). The remaining variables (2, 3, 4, 5, 8, 11, 12, 16, 19) have been calculated using a bespoke pre-processor which performed calculations on the equivalent elliptical shapes of each pore and the pore network (cf. supporting information). Figure 2 presents a simplified workflow for pore network generation. The rationale behind the use of a 2D network of pores rather than a 3D pore network skeletonization enables the network to operate on a desktop, where our networking software could extract a simplified set of 2D attributes which highlighted the key characteristics encountered during a 3D analysis. Studies have simplified the complex structure of the pores by the ellipse equivalent shape of a pore (Fournier et al., 2011), while Tsukrov (Tsukrov & Kachanov, 1993) demonstrated that elongated pores could be replaced by their ellipse-equivalent shape for DEM modelling. This network, generated for each scanned slice, was based on the arrangement and overlapping state of the 2D porosity: Each pore of a 2D slice was replaced by an ellipse of equivalent area, shape, and orientation. These ellipses were then enlarged by a constant factor. This enlarging factor, called the *area of influence*, was a computational way of representing the hydrogeological influence of a pore around its neighbourhood; or the numerical way of imaging the 3D influence of a pore on a 2D slice. The 2D arrangement of a set of links symbolized a pore network. A link set between two pores suggested the potential existence of a pathway between these two

pores in the rock. The analysis of this pore network allowed the calculation of the variables 2, 3, 4, 5, and 19, while the analysis of the ellipses defined the variables 8, 11, 12, and 16.

2.3.1.1 Pore network analysis (variables 2, 3, 4, 5, 19)

Variables 2, 3, 4, 5, and 19 are determined as follows: the area of connected pores (2) is the sum of the 2D area of the pores which are part of a connected network. The total (3), median (4) and mean length connection (5) are basic mathematical calculations using the length of every link from a 2D slice. Finally, the I/O connection (19) is a variable which is not part of the variables processed by the ANN, but rather an independent measurement used in determining the potential breakthrough location. A recursive function analyses the 2D network of links, and detects if at least one path between bottom to top of the image is found.

2.3.1.2 Ellipse analysis (variables 8, 11, 12, 16)

The ellipse shape of a pore can resolve the following variables: the ratio of pore area (8) represents the ratio between the area of the largest pore over the mean pore area of a 2D slice. This variable is used for excluding large outliers. Both the small (11) & the large (12) ellipse perimeter are calculations of both the ellipse shape of a pore and its enlarged version. The mean aspect ratio (16) is represented by the ratio of the minor axis b over the major axis a of an ellipse.

2.3.2 Signature Data Pre-processing

The signature data refers to the estimated channels magnitudes and locations. This dataset was computed from the differential result between the pre- and post-experimental scans. Our methodology involved a registration of both unaltered and altered datasets into the same 3D space, allowing us to further subtract both stacks in order to account for potential differences. Isolating and computing the dissolution channels and sub-sampling has been dine under Avizo ®9. The cuboids were re-sliced and thresholded using the Fiji *AutoTresholding* function (Schindelin et al., 2012; Ridler et al., 1978). The percentage of black and white area was calculated for each 2D slice using a batch code based on the *Measure* function under Fiji (Schindelin et al., 2012), and was used as the true solution of the channel shape and size for a set of slices of the 3D stack. The signature data were finally normalized

so that the maximum percentage area of white equals 1 (presence of dissolution channel) while the minimum was equal or close to 0 (no dissolution detected).

2.3.3 Regression and Neural Network Modelling

In this work, we trained both linear regressions and multiple hidden layer ANNs on six datasets and predicted on two, which corresponded to the four experimental regimes as explained in Section 2.1. With this network trained, we then predicted the remaining two, blind datasets' spatial channel signatures, corresponding to the remaining experimental regimes. For the four combinations of three training experimental regimes (six datasets) and one blind test experimental regime (two datasets), we performed a linear regression where eighteen normalized features were input and fitted to minimize the least-squares misfit when compared to the measured spatial channel signature extracted from before and after µCT scans, as described in Section 2.3. We did not perform any regression or model training using the I/O variable (19), which was held aside for comparison, as seen in Section 2.3.1. After the linear regression was parametrized, we performed modelling using an ANN based on the MATLAB's Deep Learning Toolbox (Hudson Beale et al., 2018), with three hidden layers, consisting of 11, 8, and 5 neurons respectively. All eighteen variables were normalized, as discussed in Section 2.3.1, before inputting into the network. All transfer functions between the input and all hidden layers in the ANN were hyperbolic tangent functions. The transfer function between the last hidden layer and the output layer was linear. Our experimental aim was to train the ANN on three experimental regimes (six datasets; three rocks), and predict channel formation on a fourth experimental regime (two datasets; one rock).

We have randomly partitioned the data from six training datasets into 74% training data and 26% validation data. We trained an ANN given this random partitioning of training and validation data and forward-modelled the spatial channel signature on the remaining two blind test datasets. This workflow has been repeated 3,000 times independently, each time training a new network given a different random partitioning of training and validation data from the same six datasets, and produced 3,000 predictions of the two blind datasets' spatial channel signatures. This amount of iteration allowed to obtain large enough outputs in reasonably short computing times (half a day for ANN training over 3,000 iterations, while predicting processing

was done within minutes). These 3,000 predictions have been made into a density plot which shows the most likely spatial channel signature, as well as the sensitivity of the network to the partitioning of input data into test and validation datasets. We performed this workflow for all four combinations of three training experimental regimes (six datasets) and one prediction experimental regime (two datasets), allowing us to simulate four, independent experiments.

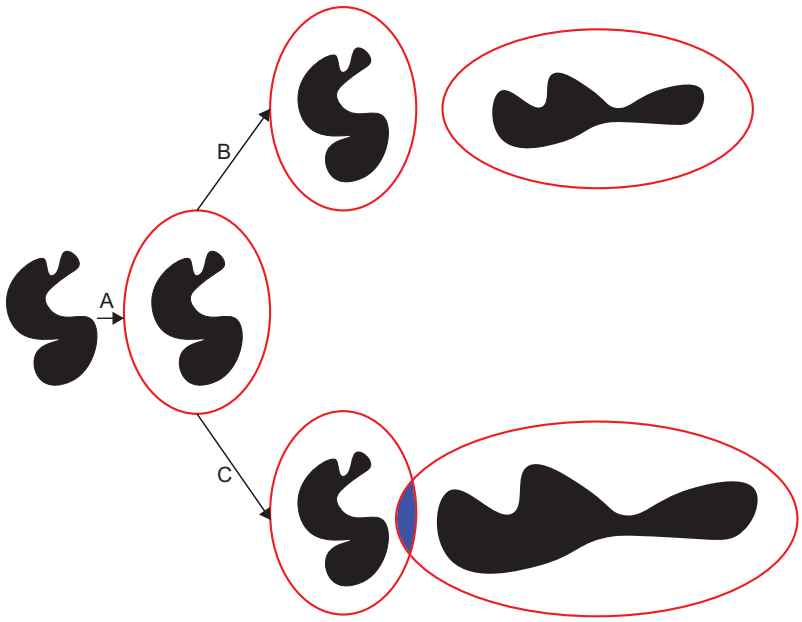

Figure 2: Steps for the detection of a link between two pores (black shapes), virtually representing a suspected connection between two pores in a rock. The step (A) represents the area of influence applied around a pore through a multiplier of the original pore area. Case (B) shows two non-overlapping pores. Case (C) displays a case of overlapping ellipses.

3 Results

3.1 Example of Post-experimental µCT Results

Figure 3 presents an example of signature from two datasets (blue curve; cf. steps C and D in Figure 1) plotted under their corresponding channel. The background greyscale images are the last image from the image stack in the Y-axis (left) and X-axis (right), and are displayed in a way to contextualize the channels in their

volumes. The cross-plotting of the thresholded percentage area of black to white of a channel offers a good insight into the location, the spread, and the magnitude of the created pore space. The values of the signature data were cross-normalized between datasets.

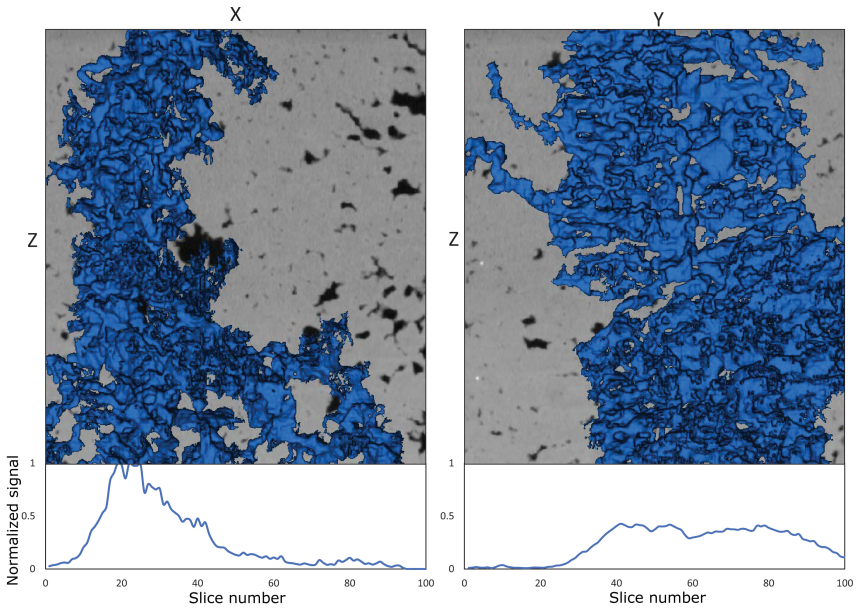

Figure 3: Example of signatures plotted under their respective cross-sectional direction for the HFR 1 experiment. Left: XZ direction; Right: YZ direction. The blue volumes represent the material removed after fluid flow through the core sample, while the plot underneath each graph represents the intensity of this material removal, per direction.

3.2 ANN Outputs

The predicted spatial channel signatures from the fitted linear regression models, as seen in Figure 5, are displayed as white curves, with the signatures measured from µCT scans displayed as red curves. Table 3 shows the percentage decrease in RMS error when predicting channel location and magnitude with the ANN over a linear regression, with values ranging from 26.5% to over 90% decrease in error. Moreover, the linear regressions model was generally ineffective at predicting spatial channel signatures. A ranking of the linear regression weights for all features is given in Table 2 and Figure 4 over all four training scenarios. In Figure 4, we show the

linear regression weights for all features. The last feature shown (19) is the size of the constant term or bias in the linear regression.

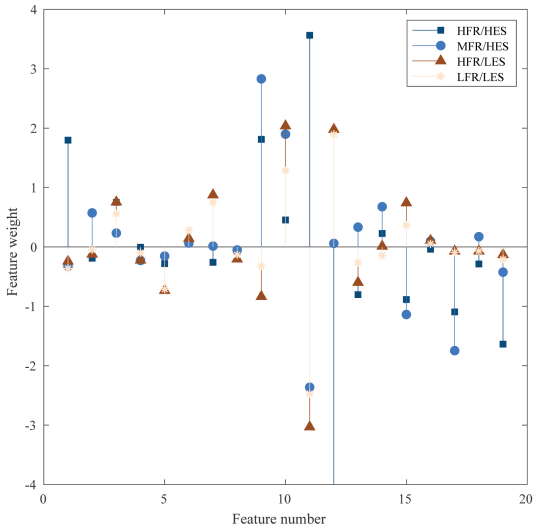

Figure 4: Linear regression weights for all features. The outlying weight on feature 12 is -6.22.

As all features were normalized before performing linear regression, we propose that features that ended with small weights were related to physical attributes which had little effect on a channel's formation. By this reasoning, we interpret that features 2, 4, 6, 8, 16, and 18 all correspond to physical properties which had little influence. These features are the area of connected pores, the median length of connections, the median pore area, the ratio of pore area, the mean ellipse aspect ratio, and the mean distance between pores. By the same reasoning as above, we interpret features with larger weights as proxies for the rocks' physical attributes which broadly exerted a stronger influence on channel formation. These features include numbers 9 to 12, which correspond to the number of pores, the mean pore perimeter, the small ellipse perimeter, and the large ellipse perimeter respectively. Of course, this reasoning of inferring feature influence on enhanced permeability of pre-existing pathway from linear regression weights is flawed as normalized features with large outliers may require large scaling to minimize their fitting residuals. Also, as we see in many cases, linear regression is not an effective predictor of channel formation on blind test data. Nevertheless, this analysis offers a crude, qualitative first estimate

of which features may or may not be important in channel formation prediction processes within heterogeneous carbonate rocks featuring macropores.

#	Key parameters	Influence
1	Total pore area	Medium
2	Area of connected pores	Low
3	Total length connection	Low
4	Median length connection	Low
5	Mean length connection	Low
6	Median pore area	Low
7	Mean pore area	Medium
8	Ratio pore area	Low
9	Number of pores	High
10	Mean pore perimeter	High
11	Small ellipse perimeter	High
12	Large ellipse perimeter	High
13	Porosity	Medium
14	Number of pore greater than mean size	Low
15	Number of pore greater than median size	Medium
16	Mean ellipse aspect ratio	Low
17	Mean distance between pores	Medium
18	Pore volume rate	Low
19	I/O connection	-

Table 2: Summary of the key parameters used in this study and their apparent relative influence on preferential channel formation.

4 Discussion

The background density plots (Figure 5) show the distribution of blind predictions generated by the 3,000 neural network simulations, given each combination of three training experimental regimes (six datasets) and one blind test experimental regime (two datasets). Intensity ranges from low (blue) to high (yellow) number of

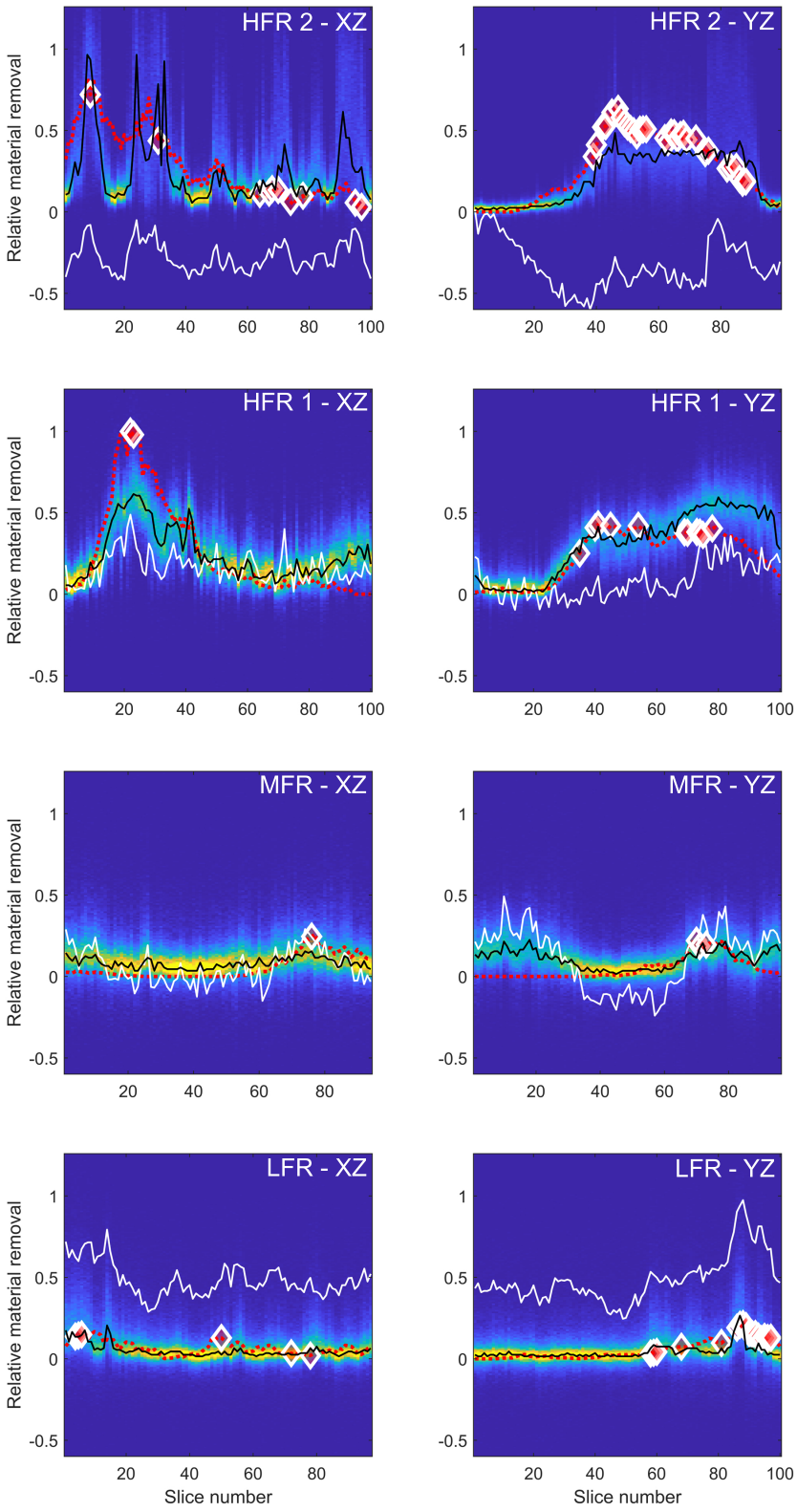

Figure 5: Measured data (red) overlain on density plot of 3,000 trained neural networks' blind test predictions for the four experiments. The white lines show the fitted linear regression models. The black lines represent the best fit for the network blind test predictions. The diamonds are the non-neural network solutions for regions of likelihood for breakthrough independently computed using variable 19 (not included in the neural network predictions).

Core name	ANN RMSE	Linear Reg. RMSE	Difference in RMSE (%)
LFR XZ	0.04	0.45	-90.6
LFR YZ	0.04	0.43	-90.2
HFR 2 YZ	0.13	0.23	-42.5
HFR 2 XZ	0.18	0.27	-35.9
HFR 1 YZ	0.11	0.66	-83.4
HFR 1 XZ	0.20	0.59	-65.7
MFR YZ	0.09	0.19	-51.3
MFR XZ	0.07	0.09	-26.5

Table 3: Percentage of the decrease in root-mean-square-error between linear regression and our ANN solution (respectively white and black lines in Figure 5). Our solution shows an increase in prediction quality of up to ∼90%.

solutions in the bins histogram. The black lines represent the averaged best solutions from our predictions. The "true" solutions (signatures) have been plotted in red on top of each result. We observed a generally effective prediction of dissolution channel location and magnitude by our approach for all four training and prediction experiments. There was a notable improvement of accuracy over the linear regression modelling. The spread in the density plot at locations with a large spatial channel signature indicated the sensitivity of neural network training to the particular, random segmentation of validation and training data. The red diamonds on Figure 5 indicate where the feature 19 has found an existing pore space connection from sample input to output in the pre-flooded rock. This single feature was an effective predictor for breakthrough and principal channel(s) location. This implied that dissolution channels are likely to occur where there is a pre-existing input/output connection in the rock before flooding. We note this feature only predicted the location, rather than the magnitude. For this reason, the use of our neural network method was beneficial over using only feature 19.

The influence of the key parameters has been assessed through an analysis of the linear regression weights for all the features processed by the ANN (Figure 4). We attributed a rank to a feature by summing, per feature, the weights of each of the

four experiments. A feature was ranked "Low" if the sum S was $\leq \quad 1$; "Medium" if $1 \leq S \leq 2$, and "High" if $S < 2$. The parameters ranked as "High" in Table 2 were assumed important as they reflected how physical (eg. fluid dynamic) and chemical variables (such as reactive transport, the acidity of the fluid, chemical interaction, etc.) could have been influenced by the surface of the pores so that the larger a pore perimeter was, the more important the wall surface in contact with the flooding fluid should have been. These effects were positively impacted by the amount of pores present. This also validated the ellipse shape assigned to each pore as a correct simplification of the general shape of a pore (Tsukrov & Kachanov, 1993; Fournier et al., 2011). We noted that the variables linked to the area of the pores were not ranking higher than "Medium" (and most often "Low"). We explained this by the relatively small importance of the area of the pores. While large pores should have driven more fluid, the large perimeter (likely associated with a large area) guaranteed more wall-fluid interaction that could have been associated with a higher degree of alteration. This was consistent with Darcy's law, where the flow will tend to be slower and residence time longer. This was possibly accentuated in the case of travertine rocks by the initial high surface roughness caused by calcite overgrowth in the pores, leading to the very high initial perimeter (although not measurable at the scale of our scans). We also believe that the ANN has made a clear distinction between porosity and number of pores, for reasons similar to that which have been explained above: a large effective porosity could have been associated with large pore areas, while the number of pores remained largely uncorrelated to the area of the pores.

5 Conclusions

This study offers a new way to accurately predict the location and shape of channels formed during water flooding in carbonates, by coupling Artificial Neural Networks (ANNs) and µCT images. A limited number of studies have already successfully linked these two tools as a segmentation method, and for rock modulus estimation, but none used ANNs for dissolution prediction. While it is commonly stated that the velocity of flow at the inlet of a core sample is the main factor for rock dissolution and/or material removal, this is only part of the story. The findings of our work showed that spatial distribution of the porosity evolution can be

predicted using only the pore network information held by the rock sample; where the micro- or macro-heterogeneities of the porous medium drive the flow instabilities to direct the fluid flow and, as such, chemical removal, towards zones of highest permeability leading to material loss. Our results showed that specific variables stand-out of the ANN analysis, and validate that geometric factors linked to the porosity and pore shape of a rock contain, most of the time, the necessary data for predicting material loss during rock-water flooding. If a linear combination of these µCT-extracted attributes can successfully predict a rock's spatial channel signature, the weights from the linear regression could be considered indicators of the influence of µCT-extracted feature in channel formation. While this statement is valid in heterogeneous travertine rocks, we remain careful with other types of carbonate, or even other types of lithology which have not been tested in this study.

Acknowledgments

The authors would like to thank Petrobras and Shell for their sponsorship of the International Centre for Carbonate Reservoirs (ICCR), and for permission to publish this work from the GeoMeChem project.

The data used in this work are available at the following address: `https://doi.org/10.6084/m9.figshare.c.5335454` (Brondolo et al., 2021).

References

Basheer, I. A., & Hajmeer, M. (2000). Artificial neural networks: fundamentals, computing, design, and application. *Journal of microbiological methods*, *43*(1), 3–31.

Bazin, B., Roque, C., Bouteca, M., et al. (1995). A laboratory evaluation of acid propagation in relation to acid fracturing: Results and interpretation. In *Spe european formation damage conference*. Society of Petroleum Engineers.

Bijeljic, B., Muggeridge, A. H., & Blunt, M. J. (2004). Pore-scale modeling of longitudinal dispersion. *Water Resources Research*, *40*(11).

Blunt, M. J., Bijeljic, B., Dong, H., Gharbi, O., Iglauer, S., Mostaghimi, P., ... Pentland, C. (2013). Pore-scale imaging and modelling. *Advances in Water Resources*, *51*, 197–216.

Brondolo, F., Cilli, P., Fraser-Harris, A., Butler, I., Edlmann, K., & McDer-

mott, C. (2021, Mar). *Machine learning based prediction of channelisation during dissolution of carbonate rocks.* figshare. Retrieved from https://figshare.com/collections/Machine_learning_based_prediction_of_channelisation_during_dissolution_of_carbonate_rocks/5335454/1 doi: 10.6084/m9.figshare.c.5335454

Budek, A., & Szymczak, P. (2012). Network models of dissolution of porous media. *Physical Review E*, *86*(5), 056318.

Buijse, M., et al. (1997). Mechanisms of wormholing in carbonate acidizing. In *International symposium on oilfield chemistry.* Society of Petroleum Engineers.

Chauhan, S., Rühaak, W., Khan, F., Enzmann, F., Mielke, P., Kersten, M., & Sass, I. (2016). Processing of rock core microtomography images: Using seven different machine learning algorithms. *Computers & Geosciences*, *86*, 120–128.

Chen, Y., Fambrough, J., Bartko, K., Li, Y., Montgomery, C., Ortoleva, P., et al. (1997). Reaction-transport simulation of matrix acidizing and optimal acidizing strategies. In *International symposium on oilfield chemistry.* Society of Petroleum Engineers.

Cortina-Januchs, M., Quintanilla-Dominguez, J., Vega-Corona, A., Tarquis, A., & Andina, D. (2011). Detection of pore space in ct soil images using artificial neural networks. *Biogeosciences*, *8*(2), 279–288.

Daccord, G., Lenormand, R., & Lietard, O. (1993). Chemical dissolution of a porous medium by a reactive fluid—i. model for the "wormholing" phenomenon. *Chemical Engineering Science*, *48*(1), 169–178.

Daccord, G., Lietard, O., & Lenormand, R. (1993). Chemical dissolution of a porous medium by a reactive fluid—ii. convection vs reaction, behavior diagram. *Chemical engineering science*, *48*(1), 179–186.

Daccord, G., Touboul, E., Lenormand, R., et al. (1989). Carbonate acidizing: toward a quantitative model of the wormholing phenomenon. *SPE production engineering*, *4*(01), 63–68.

Dierick, M., Masschaele, B., & Van Hoorebeke, L. (2004). Octopus, a fast and user-friendly tomographic reconstruction package developed in labview®. *Measurement Science and Technology*, *15*(7), 1366.

Fournier, F., Leonide, P., Biscarrat, K., Gallois, A., Borgomano, J., & Foubert, A. (2011). Elastic properties of microporous cemented grainstones. *Geophysics*,

400 *76*(6), E211–E226.

401 Fredd, C., Fogler, H. S., et al. (1996). Alternative stimulation fluids and their im-
402 pact on carbonate acidizing. In *Spe formation damage control symposium.* So-
403 ciety of Petroleum Engineers.

404 Fredd, C. N., & Fogler, H. S. (1998). Influence of transport and reaction on worm-
405 hole formation in porous media. *AIChE journal*, *44*(9), 1933–1949.

406 Frick, T., Mostofizadeh, B., Economides, M., et al. (1994). Analysis of radial core
407 experiments for hydrochloric acid interaction with limestones. In *Spe formation*
408 *damage control symposium.* Society of Petroleum Engineers.

409 Golfier, F., Zarconne, C., Bazin, B., Lenormand, R., Lasseux, D., & QUINTARD,
410 M. (2002). On the ability of a darcy-scale model to capture wormhole forma-
411 tion during the dissolution of a porous medium. *Journal of fluid Mechanics*,
412 *457*, 213–254.

413 Hoefner, M., & Fogler, H. S. (1988). Pore evolution and channel formation during
414 flow and reaction in porous media. *AIChE Journal*, *34*(1), 45–54.

415 Huang, T., Hill, A., Schechter, R., et al. (1997). Reaction rate and fluid loss: the
416 keys to wormhole initiation and propagation in carbonate acidizing. In *Inter-*
417 *national symposium on oilfield chemistry.* Society of Petroleum Engineers.

418 Huang, T., Zhu, D., & Hil, A. (1999). Prediction of wormhole population density in
419 carbonate matrix acidizing. In *Spe european formation damage conference.* So-
420 ciety of Petroleum Engineers.

421 Hudson Beale, M., Hagan, M. T., & Demuth, H. B. (2018). *Impress - supporting ed-*
422 *ucation across europe.* Retrieved from `https://uk.mathworks.com/help/pdf`
423 `_doc/deeplearning/nnet_ref.pdf`

424 Hung, K., Hill, A., Sepehrnoori, K., et al. (1989). A mechanistic model of wormhole
425 growth in carbonate matrix acidizing and acid fracturing. *Journal of petroleum*
426 *technology*, *41*(01), 59–66.

427 Liu, X., Ormond, A., Bartko, K., Ying, L., & Ortoleva, P. (1997). A geochemical
428 reaction-transport simulator for matrix acidizing analysis and design. *Journal*
429 *of Petroleum Science and Engineering*, *17*(1-2), 181–196.

430 Luquot, L., Hebert, V., & Rodriguez, O. (2016). Calculating structural and geomet-
431 rical parameters by laboratory measurements and x-ray microtomography: a
432 comparative study applied to a limestone sample before and after a dissolution

433 experiment. *Solid Earth*, *7*(2).

434 Menke, H., Bijeljic, B., & Blunt, M. (2017). Dynamic reservoir-condition microto-
435 mography of reactive transport in complex carbonates: Effect of initial pore
436 structure and initial brine ph. *Geochimica et Cosmochimica Acta*, *204*, 267–
437 285.

438 Ridler, T., Calvard, S., et al. (1978). Picture thresholding using an iterative selection
439 method. *IEEE transactions on Systems, Man and Cybernetics*, *8*(8), 630–632.

440 Schindelin, J., Arganda-Carreras, I., Frise, E., Kaynig, V., Longair, M., Pietzsch, T.,
441 ... others (2012). Fiji: an open-source platform for biological-image analysis.
442 *Nature methods*, *9*(7), 676.

443 Sonmez, H., Gokceoglu, C., Nefeslioglu, H., & Kayabasi, A. (2006). Estimation of
444 rock modulus: for intact rocks with an artificial neural network and for rock
445 masses with a new empirical equation. *International Journal of Rock Mechan-*
446 *ics and Mining Sciences*, *43*(2), 224–235.

447 Steefel, C. I., & Lasaga, A. C. (1990). Evolution of dissolution patterns. In *Chemical*
448 *modeling of aqueous systems ii* (p. 212-225). American Chemical Society. Re-
449 trieved from `https://pubs.acs.org/doi/abs/10.1021/bk-1990-0416.ch016`
450 doi: 10.1021/bk-1990-0416.ch016

451 Terzaghi, K. (1951). *Theoretical soil mechanics*. Chapman And Hall, Limited.; Lon-
452 don.

453 Tsukrov, I., & Kachanov, M. (1993). Solids with holes of irregular shapes: effective
454 moduli and anisotropy. *International Journal of Fracture*, *64*(1), R9–R12.

455 Walle, L., Papamichos, E., et al. (2015). Acidizing of hollow cylinder chalk speci-
456 mens and its impact on rock strength and wormhole network structure. In *49th*
457 *us rock mechanics/geomechanics symposium*. American Rock Mechanics Asso-
458 ciation.

459 Wang, Y., Hill, A., Schechter, R., et al. (1993). The optimum injection rate for ma-
460 trix acidizing of carbonate formations. In *Spe annual technical conference and*
461 *exhibition*. Society of Petroleum Engineers.